

AD-A092 025

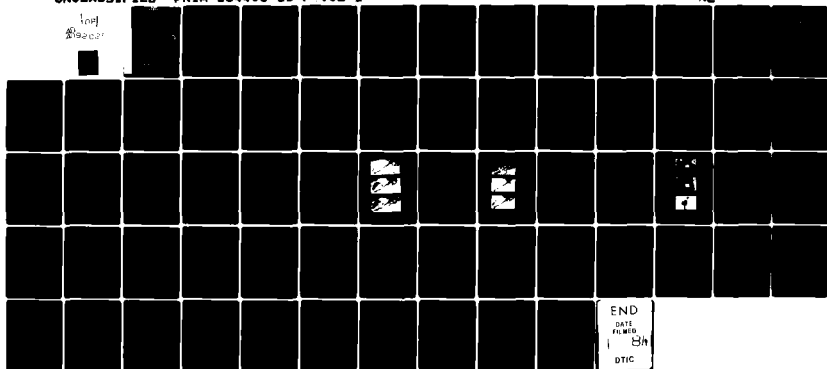
ENVIRONMENTAL RESEARCH INST OF MICHIGAN ANN ARBOR AP--ETC F/G 8/10
COASTAL REMOTE SENSING INVESTIGATIONS, VOLUME 1. MARINE ENVIRON--ETC(U
APR 80 D R LYZENG
N00014-78-C-0458

UNCLASSIFIED

FRIM-134400-11-F-VOL-1

NL

100
000000



END
DATE
FILMED
DTIC

LEVEL

12

134400-11-F

Final Technical Report
**COASTAL REMOTE SENSING
INVESTIGATIONS**

Volume 1: Marine Environment

DAVID R. LYZENG
Applications Division

APRIL 1980

AD A092025

DTIC
SELECTED
NOV 18 1980

Office of Naval Research
Geography Programs
Arlington, VA 22217
Contract No. N00014-78-C-0458

DISTRIBUTION STATEMENT A
Approved for public release;
Distribution Unlimited

DC FILE COPY

ENVIRONMENTAL
RESEARCH INSTITUTE OF MICHIGAN
BOX 8618 • ANN ARBOR • MICHIGAN 48107

80 9 29 12g

Unclassified

SECURITY CLASSIFICATION OF THIS PAGE (When Data Entered)

REPORT DOCUMENTATION PAGE		READ INSTRUCTIONS BEFORE COMPLETING FORM
1 REPORT NUMBER 134400-11-F	2 GOVT ACCESSION NO AD -4092 025	3 RECIPIENT'S CATALOG NUMBER
4 TITLE (and Subtitle) COASTAL REMOTE SENSING INVESTIGATIONS, VOLUME 1, MARINE ENVIRONMENT.		5 TYPE OF REPORT & PERIOD COVERED FINAL TECHNICAL REPORT 3/1/78 to 4/30/80
7 AUTHOR(s) David R. Lyzenga		6 PERFORMING ORG REPORT NUMBER 134400-11-F-VOL-1
9 PERFORMING ORGANIZATION NAME AND ADDRESS Environmental Research Institute of Michigan Applications Division, Box 8618 Ann Arbor, MI 48107		8 CONTRACT OR GRANT NUMBER (if) N00014-78-C-0458
11 CONTROLLING OFFICE NAME AND ADDRESS Office of Naval Research Geography Programs Arlington, VA 22217		10 PROGRAM ELEMENT PROJECT TASK AREA & WORK UNIT NUMBERS C-1641
14 MONITORING AGENCY NAME AND ADDRESS (if different from Controlling Office)		12 REPORT DATE APR 1980
		13 NUMBER OF PAGES vi + 56
		15 SECURITY CLASS (of this report) Unclassified
16 DISTRIBUTION STATEMENT (of this Report)		15a DECLASSIFICATION/DOWNGRADING SCHEDULE
<div style="border: 1px solid black; padding: 5px; text-align: center;"> DISTRIBUTION STATEMENT A Approved for public release; Distribution Unlimited </div>		
17 DISTRIBUTION STATEMENT (of the abstract entered in Block 20, if different from Report)		
18 SUPPLEMENTARY NOTES		
19 KEY WORDS (Continue on reverse side if necessary and identify by block number) Remote Sensing Water Attenuation Bottom Reflectance Radiative Transfer		
20 ABSTRACT (Continue on reverse side if necessary and identify by block number) Algorithms for the extraction of water attenuation and bottom reflectance parameters in shallow water from remote sensing data are described and evaluated. Assuming water parameters are uniform, relative water attenuation coefficients can be extracted from passive data and absolute attenuation coefficients can be obtained from active/passive scanner data. Bottom reflectance variations can be mapped using passive multispectral scanner data. →		

DD FORM 1 JAN 73 1473 EDITION OF 1 NOV 65 IS OBSOLETE

Unclassified

SECURITY CLASSIFICATION OF THIS PAGE (When Data Entered)

Unclassified

SECURITY CLASSIFICATION OF THIS PAGE (When Data Entered)

20. ABSTRACT (Continued from previous page)

Preliminary development of a Monte Carlo radiative transfer model has begun. A new approximate radiative transfer model has also been developed and the results are compared with exact calculations and with the results of the quasi-single-scattering (QSS) and double-delta (Turner) models.

Unclassified

SECURITY CLASSIFICATION OF THIS PAGE (When Data Entered)

CONTENTS

1. Introduction	1
2. Water Properties	3
2.1 Passive Methods	3
2.2 Active Methods	13
3. Bottom Features	23
3.1 Data Analysis	23
3.2 Evaluation of Results	29
4. Radiative Transfer Modeling	35
4.1 Water Modeling	35
4.2 Atmospheric Modeling	36
5. Conclusions and Recommendations	47
APPENDIX A: FORTRAN Code for Monte Carlo Model	50
APPENDIX B: FORTRAN Code for Approximate Models	55
References	57

Accession For
 NITS SHOT
 FIVE TAP
 Unrecorded
 Justification
 Distribution
 Approved for
 Release
 A

LIST OF FIGURES

<u>FIGURE</u>	<u>TITLE</u>	<u>PAGE</u>
1	Scatter plot of X_i values for aircraft bands C5 and C7 over two bottom types	5
2	Map of North Cat Cay Test Site	7
3	Scatter plot of X_i values for Landsat bands MSS4 and MSS5 over sand bottom	11
4	Underwater irradiances measured with filtered photometer at two locations on the Great Bahama Bank	12
5	Plot of returned laser pulse in shallow water near North Cat Cay	14
6	(a) Passive signals in band C8 versus depth	16
	(b) Passive signals in band C6 versus depth	17
	(c) Passive signals in band C4 versus depth	18
7	Comparison of irradiance attenuation coefficients obtained from M-8 scanner with values measured <u>in situ</u>	20
8	Amplitude of bottom-reflected laser pulse versus depth	22
9	Images generated from M-8 aircraft scanner data	26
10	Images generated from Landsat data	28
11	Underwater photographs at stations B1, B2, and C2	31
12	Measured bottom reflectance versus Y_1 value from aircraft and Landsat data	33
13	Phase function used by Hansen for reflectance calculations	40
14	Comparison of QSS model with exact calculations	41
15	Comparison of double-delta model with exact calculations	43
16	Comparison of iterated Eddington model with exact calculations	46

LIST OF TABLES

<u>TABLE</u>	<u>TITLE</u>	<u>PAGE</u>
1	Spectral bands recorded by M-8 scanner system	8
2	Ratios of water attenuation coefficients determined from aircraft MSS data	9
3	Irradiance attenuation coefficients measured by photometer	13
4	Attenuation coefficients obtained from M-8 scanner data	19
5	Summary of bottom observations at test locations	30
6	Bottom-type indices calculated from aircraft and Landsat data at test locations	32

ACKNOWLEDGEMENTS

The research described in this report is closely related to the problem of water depth extraction from remote sensing data. This problem has been investigated by Mr. Fabian Polcyn of the Environmental Research Institute of Michigan for several years, most recently under the sponsorship of the Defense Mapping Agency (contract numbers DMA 800-77-C-0053 and DMA 800-78-C-0060). A mutual interchange of information and stimulation has occurred between these programs, and two field trips organized as a part of the DMA program were participated in by the author of this report under ONR support. The aircraft data used in this study was also collected under DMA sponsorship and was released in exchange for surface truth measurements made under ONR support.

In connection with the field measurement program, the assistance of Mr. Robert A. Shuchman in making the underwater measurements and photography, and Mr. James Hillier in providing logistical support, is hereby acknowledged. The author also wishes to thank Mr. Fred Tanis for discussions regarding the Monte Carlo model and Mr. Anthony LaRocca for advice and support in the atmospheric modeling efforts described in this report.

1.0

INTRODUCTION

This report summarizes work done on contract N00014-78-C-0458 during the period 3-1-78 to 4-30-80, concentrating especially on the parts of the program dealing with the marine environment during the last year of the contract. Efforts on the beach environment tasks during the last year are summarized in a separate report (no. 134400-12-F), and results obtained during the first year of the contract are described in report no. 134400-7-T. Various aspects of the technical work have also been reported in papers submitted to Remote Sensing of Environment and the IEEE Transactions on Geoscience and Remote Sensing. The technical monitor for this contract was Mr. Hans Dolezalek. The principal investigator was Dr. David Lyzenga and the project manager was Mr. Fred Thomson.

Three areas of research are described in this report. The first deals with the extraction of water optical properties from remote sensing data, including both passive (satellite and aircraft) data and active (aircraft) data. These properties are needed for use by the bottom recognition and water depth algorithms, and may have independent applications as well. The second topic is a further evaluation of the bottom recognition algorithm using both Landsat and aircraft data over a test site near North Cat Cay in the Bahamas. The third topic deals with radiative transfer modeling as applied to water and atmospheric problems. A Monte Carlo model has been developed which is capable of accurate solutions and of modification for complex geometries and boundary conditions, but requires a fairly large expenditure of computer time. Secondly, a re-evaluation of several approximate models has been conducted, including the quasi-single-scattering (QSS) model which has been used in the past for water reflectance calculations and the double-delta (Turner) model which has been used for atmospheric

calculations. Recently a rather serious deficiency has been discovered in the Turner model which causes an overestimate of the path radiance in the antisolar direction. The QSS model appears to give adequate results for the conservative scattering case with small optical thickness but breaks down for larger values of the optical thickness. A new model has been developed which shares certain similarities with both the Turner and QSS models but gives somewhat better results for the conservative scattering case, particularly for large optical depths.

2.0

WATER PROPERTIES

2.1. PASSIVE METHODS

The basis for the methods of processing passive shallow-water remote sensing data described in this report is the assumption of an exponential depth dependence of the observed bottom-reflected radiances. The rationale for this assumption has been discussed in previous reports [1,2], and no overwhelming evidence has been found to the contrary, although it is certain to break down in areas where the optical properties of the water are changing rapidly. In areas where horizontal mixing ensures a relatively homogeneous composition of the water, however, the assumption appears to be justified. Thus, when the measured radiances are transformed according to the following equation

$$X_i = \ln(L_i - L_{si}) \quad (1)$$

where L_i is the measured radiance in band i and L_{si} is the deep-water radiance, the resulting variables are linear functions of the water depth and are linearly related to each other, for a given bottom reflectance. That is, if X_i is plotted versus X_j and the water depth is varied, the data points will fall along a straight line whose slope is K_i/K_j , where K_i is the irradiance attenuation coefficient of the water in band i . If the bottom reflectance is changed, the data points will fall along a parallel line which is displaced from the first by an amount proportional to the change in reflectance.

This suggests a procedure for obtaining water attenuation parameters from shallow-water MSS data. If a set of radiance measurements are made over an area of variable depth but uniform bottom reflectance, a linear correlation would be expected between any two of the variables

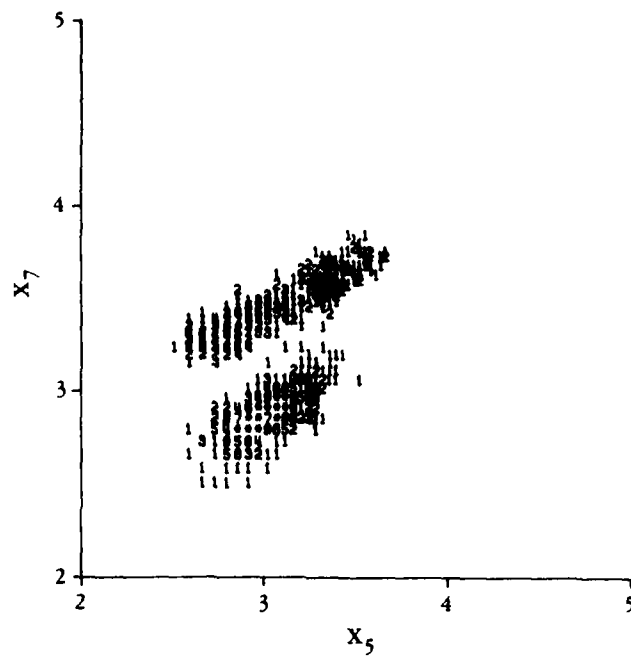
X_i and X_j . A regression analysis of this data would then yield the ratio of the attenuation coefficients in the two wavelength bands used. This procedure does not yield the correct results, however, if the bottom reflectance varies with depth within the area selected. Thus, the problem is to select an area of uniform bottom reflectance for the analysis. This selection process is directly analogous to the process of training set selection in conventional supervised classification techniques used in remote sensing. The selection may be done on the basis of field observations and/or photographic interpretation using color aerial photography. Alternatively, an analysis of the self-consistency of the data can be done to determine the uniformity of the training set. In this case, a uniform bottom is indicated by a high correlation among the X_i variables, and this condition can usually be identified by an inspection of scatter plots of the data. Figure 1a shows a scatter plot of X_i values over an area containing a mixture of bottom types, while Figure 1b shows the distribution of the same variables over a uniform sand bottom.

Having selected a training set, a conventional least-squares regression analysis may be done to determine the ratio of attenuation coefficients. The disadvantage of this procedure, however, is that the results depend upon the order in which variables are selected, since the mean square deviation from the regression line is calculated in the direction of the dependent variable. A better procedure is to determine the line for which the mean square deviation measured perpendicular to the line is minimized. This procedure results in the equation

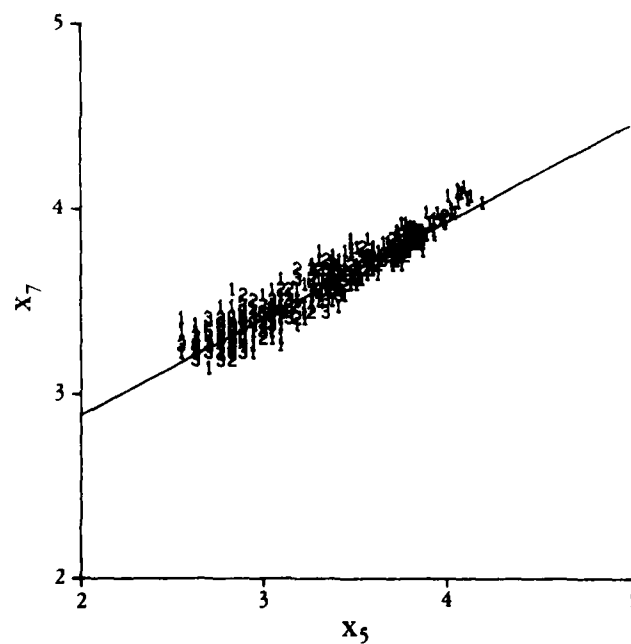
$$K_i/K_j = a + \sqrt{a^2 + 1} \quad (2)$$

where

$$a = \frac{\sigma_{ii} - \sigma_{jj}}{2\sigma_{ij}} \quad (3)$$



(a) mixture of sand and vegetation



(b) sand (line indicates least-squares fit to data)

Figure 1. Scatter plot of X_1 values for aircraft bands C5 (.58-.64 μm) and C7 (.52-.57 μm) over two bottom types. X_1 is log of bottom-reflected signal.

and
$$\sigma_{ij} = \overline{X_i X_j} - \overline{X_i} \overline{X_j} \quad (4)$$

(i.e., σ_{ii} is the variance of the X_i measurements, σ_{jj} is the variance of the X_j measurements, and σ_{ij} is the covariance of X_i and X_j). This equation yields a result which does not depend on the order in which the variables are selected.

This procedure has been tested with two data sets collected near North Cat Cay in the Bahamas. The test site selected for this evaluation is located on the western edge of the Great Bahama Bank, about 90 km east of Miami, Florida, and 15 km south of Bimini. The bottom in this area is composed largely of white carbonate sand with some rock and coral formations, and heavy growths of vegetation (mainly Thalassia) in protected areas. The water is very clear, and extensive shallow areas exist with depths ranging from 1 to 15 meters, dropping off to very great depth at the edge of the Bank. A map of the test site is shown in Figure 2.

Measurements of the irradiance attenuation coefficient of the water were made at several locations in the Great Bahama Bank in October 1977, using Kahl submarine photometer with filters approximating the Landsat green (MSS4, 0.5-0.6 μm) and red (MSS5, 0.6-0.7 μm) bands. Two of these measurements were taken near the North Cat Cay test site, on October 4 and 5, 1977. Landsat data was also collected over the test site on October 11, 1977. The Landsat MSS data was collected in high gain mode and exhibits a large amount of striping, which was corrected prior to the processing described in this report.

The test site was revisited in August, 1978, at which time a set of observations of the bottom type and water depth were made at nine stations around North Cat Cay. Underwater photographs were taken and were subsequently analyzed in order to extract the bottom reflectance at each station. Aircraft MSS data was also collected at this time

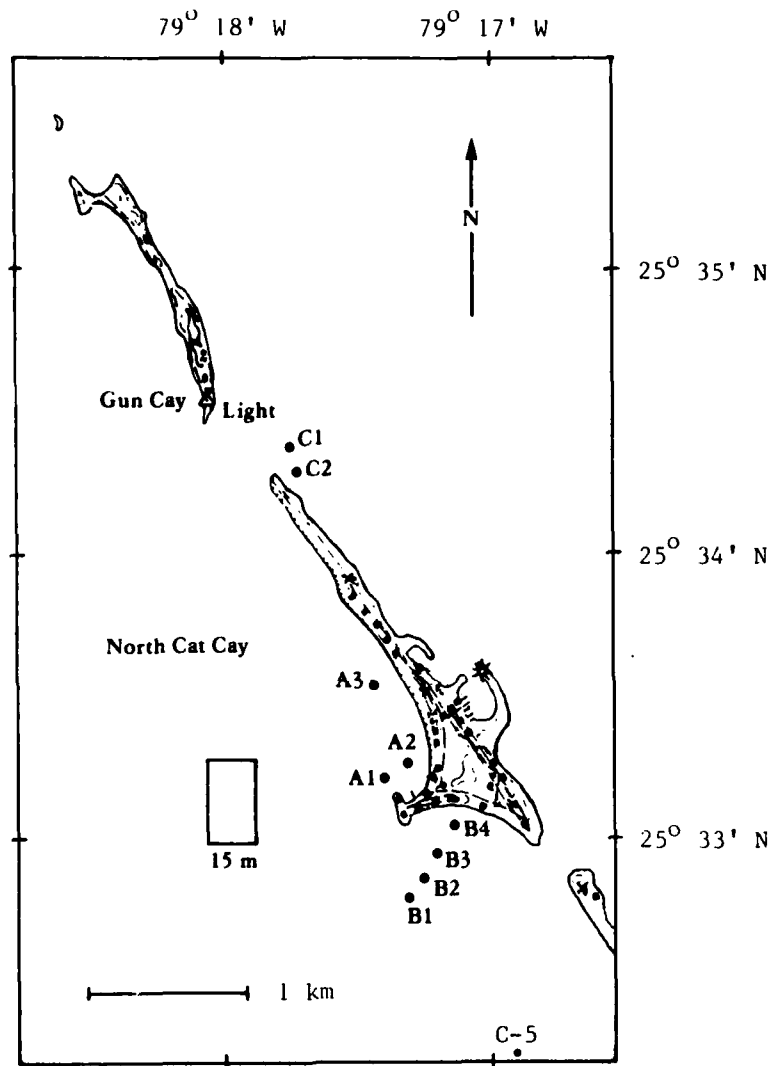


Figure 2. Map of North Cat Cay test site. C5 indicates location of water attenuation measurements, and other labelled dots indicate bottom reflectance measurement stations (c.f., section 3.2). Box labelled "15m" indicates area of 15 meters depth.

using the ERIM M-8 multispectral scanner system. This data was collected at an altitude of 3.3 km, with a spatial resolution of approximately 8 meters, as compared to the Landsat spatial resolution of 79 meters. The spectral resolution of the aircraft scanner was also somewhat higher than the Landsat MSS, with bandwidths on the order of 0.05 μm for the wavelengths bands used. The aircraft data included some sun glint and path radiance effects, which were removed during a pre-processing step.

The aircraft MSS records a digital signal which is proportional to the radiance at each point in the scene. The radiance within each of the spectral bands indicated in Table 1 is recorded separately, and with a different proportionality constant depending on the gain settings selected by the operator. The proportionality constants relating the digital signals to the radiances in each band could be determined by an analysis of the calibration data recorded by the MSS, but since the water attenuation algorithm does not require absolute radiances this calibration was not attempted.

TABLE 1
SPECTRAL BANDS RECORDED BY M-8 SCANNER SYSTEM

<u>Band Designation</u>	<u>Wavelength (μm)</u>
C9	.48-.52
C8	.50-.54
C7	.52-.57
C6	.55-.60
C5	.58-.64
C4	.62-.70
C2	.67-.94
A1	thermal IR

The first step in the analysis procedure is to determine the deep-water signals. This is accomplished by averaging the signals over a portion of the scene within which the contribution due to bottom reflectance is negligible. For the scene under consideration such an area was easily located off the edge of the Bank where the water depths are on the order of several hundred meters.

Having determined the deep-water signals the X_i variables were computed and scatter plots similar to those shown in Figure 1 were generated for each band pair. Scatter plots were generated for several areas in an attempt to locate an area of homogeneous bottom, as indicated by the linear distribution shown in Figure 1b, which was obtained from an area just west of North Cat Cay. Ratios of the water attenuation coefficients were then calculated as outlined in the preceding section. The results are shown in Table 2. Unfortunately, no in situ water optical measurements were made at the time of the overflight, but the ratios shown in Table 2 are within the range expected for oceanic water.

TABLE 2
RATIOS OF WATER ATTENUATION COEFFICIENTS
DETERMINED FROM AIRCRAFT MSS DATA

<u>Band Pair</u>	<u>Ratio of Attenuation Coefficients</u>
C9/C4	0.28
C8/C4	0.29
C7/C4	0.33
C6/C4	0.37
C5/C4	0.64

Analysis of the Landsat data set for frame 2993-14385 proceeded in a similar manner to the aircraft data set. Deep water signals were calculated for an area off the edge of the Bank west of North Cat Cay, and scatter plots of X_1 (MSS 4) versus X_2 (MSS 5) were generated for several areas. Due to the coarser spatial resolution, areas of uniform bottom type are somewhat more difficult to find, and the set of useable data points is smaller. Figure 3 shows a scatter plot for an area south of North Cat Cay which appears to be relatively homogeneous. The ratio of attenuation coefficients (K_4/K_5) obtained from this set of points is 0.24.

The results of the water optical parameter determination may be evaluated by a comparison with field measurements of the irradiance attenuation coefficient. Unfortunately, no exactly simultaneous field data are available. However, as mentioned earlier, two measurements were made near the test site within a week of the Landsat overpass, which indicate at least the range of attenuation coefficients occurring there. The first measurement was made on October 4, 1977 just south of North Cat Cay (Station C-5, $25^{\circ} 32.2'N$, $70^{\circ} 16.9'W$) while the second measurement was made on the following day west of Bimini (Station D-7, $25^{\circ} 43.9'N$, $79^{\circ} 18.2'W$). The irradiance measurement in the two wavelength bands are shown in Figure 4, and the attenuation coefficients derived from the measurements are shown in Table 3. The higher attenuation at D-7 is thought to be due to resuspension of sediments during high wind conditions occurring on the 4th and 5th of October. Winds were calm prior to the Landsat overpass and the attenuation coefficients probably returned to the values measured at C-5. The ratio of attenuation coefficients extracted from the Landsat data was 0.24, which is within ten percent of the measured value at C-5. The ratio of attenuation coefficients obtained from the aircraft data for a similar pair of wavelength bands (C7 and C4) was 0.33, which is

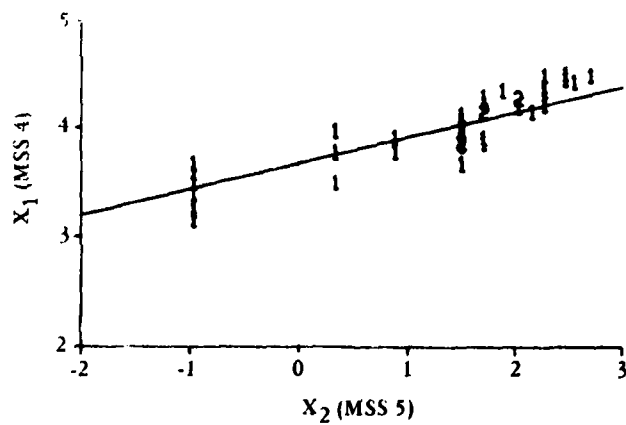


Figure 3. Scatter plot of X_i values for Landsat bands MSS4 (.5-.6 μm) and MSS5 (.6-.7 μm) over sand bottom south of North Cat Cay. X_i is log of bottom-reflected signal.

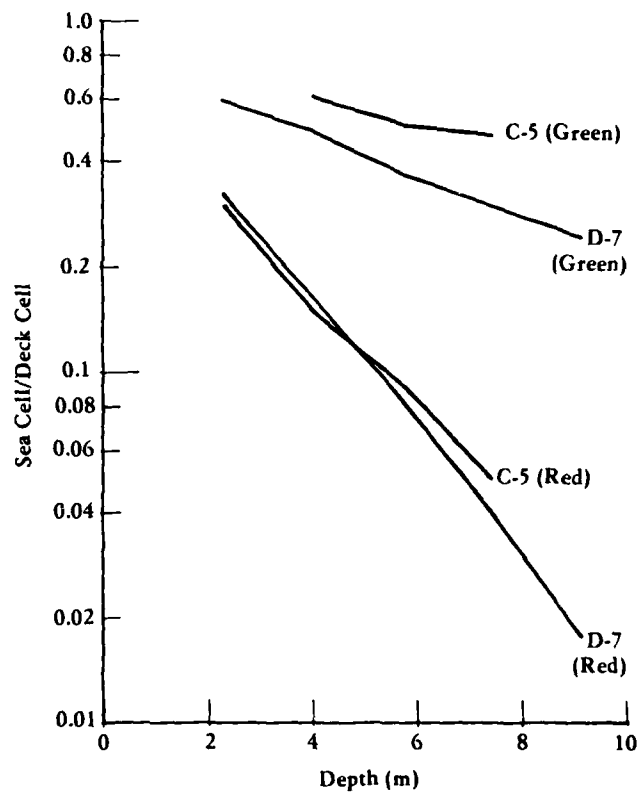


Figure 4. Underwater irradiances measured with filtered photometer at two locations on the Great Bahama Bank. Green filter corresponds to Landsat band MSS4 and red filter corresponds to MSS5. Underwater irradiances (measured by "sea cell") were normalized by above-surface irradiances ("deck cell") in order to compensate for illumination changes.

closer to the value measured at Station D-7. Since the aircraft data was collected some 10 months later, not too much significance can be placed on this comparison, but the attenuation parameters obtained from the aircraft data analysis are apparently within reasonable limits.

TABLE 3
IRRADIANCE ATTENUATION COEFFICIENTS
MEASURED BY PHOTOMETER NEAR TEST SITE

Station	Date	Location	Green Filter (MSS4)	Red Filter (MSS5)	Ratio
C-5	10/4/77	25° 32.3'N, 79° 16.9'W	.080 m ⁻¹	.352 m ⁻¹	.227
D-7	10/5/77	25° 43.9'N, 79° 18.2'W	.134 m ⁻¹	.408 m ⁻¹	.328

2.2 ACTIVE METHODS

In addition to the collection of passive data (reflected sunlight), the ERIM M-8 scanner is capable of active operation using a pulsed-laser source. The characteristics of this device have been described by Hasell *et al* [3]. Basically, a narrow pulse of light is transmitted downward and the time history of the reflected pulse is recorded using a transient digitizer. The transmitted pulse is timed and directed to correspond to a known pixel location in the passive data. Over shallow water, the returned pulse has recognizable components due to reflection from the water surface and from the ocean bottom (c.f. Figure 5). Thus, the difference in the time of arrival of these pulses can be measured and used to accurately calculate the water depth.

Having a set of depth measurements at known locations in the passive data, a regression analysis can be performed between the depths

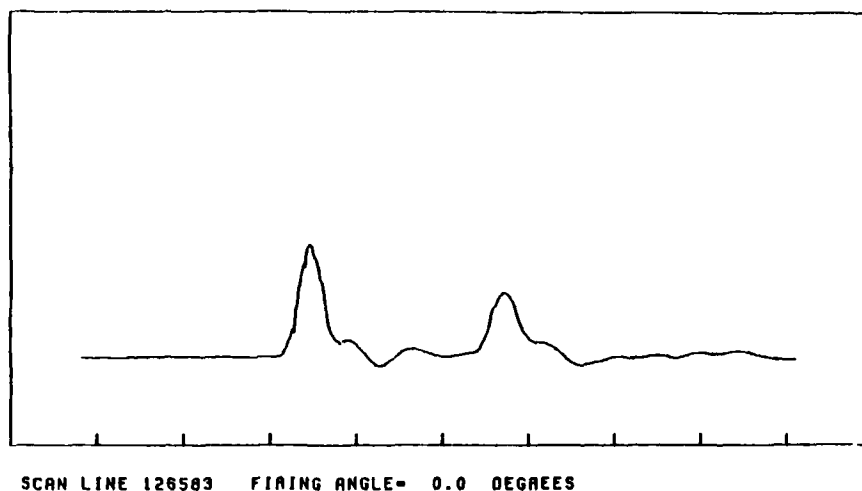


Figure 5. Plot of amplitude of reflected laser pulse versus time (horizontal axis) over shallow water near North Cat Cay. Incident pulse was emitted vertically downward from aircraft. Surface-reflected pulse is on the left, bottom-reflected pulse is to the right. Time scale is 20 ns/division.

and the passive signals in order to extract absolute water attenuation coefficients for the passive bands. As in the case of the passive method described in section 2.1, this procedure required a set of points over a fairly uniform bottom, which can be identified by an examination of the internal consistency of the data aided by photo interpretation or field observations of the scene.

This procedure was tested using data from a second aircraft run over the North Cat Cay test site at an altitude of 300 meters with the pulsed laser in operation. Water depths were obtained from the pulsed laser data over a set of 30 points identified as sand south of North Cat Cay. The passive data values at the corresponding locations were then extracted and the X_i variables (c.f. equation 1) calculated for each band. Plots of these variables versus depth for three of the passive bands (C3, C6, and C4) are shown in Figures 6 (a) - (c). Regression analyses were carried out for each band to yield a set of equations

$$X_i = a_i - b_i Z \quad (5)$$

where i is the band number. On the basis of the reflectance models discussed in earlier reports [1,2], the slope of the regression line (b_i) may be taken as approximately twice the irradiance attenuation coefficient (K_i). The values of K_i obtained from this analysis are listed in Table 4 and are plotted versus wavelength in Figure 7. Also included on this plot are the attenuation coefficients tabulated by Jerlov [4] for water types II and III, and the measured values discussed in section 2.1. Agreement among these sets of values is quite good, although the increase in K with wavelength is somewhat smaller for the remote sensing values than for the in situ measurements or the Jerlov values. The ratios of the K values shown in Table 4 are also quite consistent with those obtained passively (c.f. Table 2)

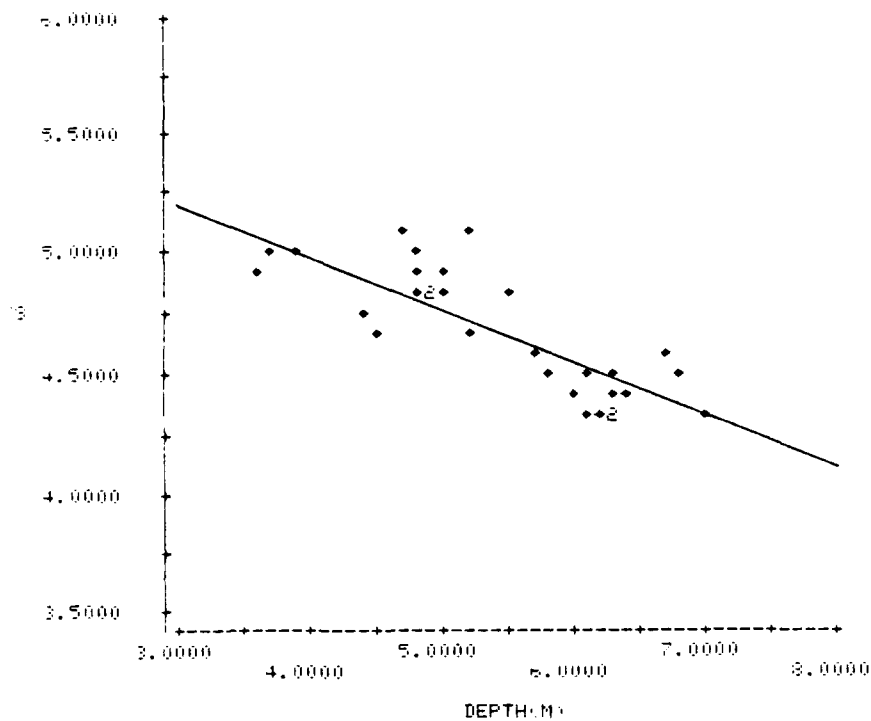


Figure 6a. Passive signals in band C8 versus depth. Vertical axis is log of bottom-reflected signal. Line indicates least-squares fit. Scatter of measured values is due to differences in bottom reflectance.

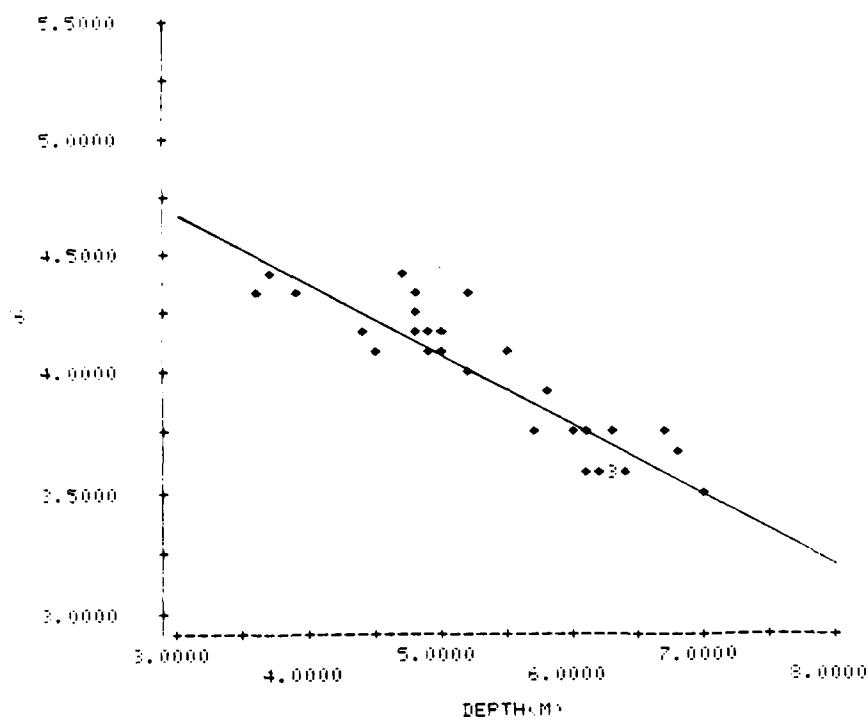


Figure 6b. Passive signals in band C6 versus depth. Vertical axis is log of bottom-reflected signal. Line indicates least-squares fit. Scatter of measured values is due to differences in bottom reflectances.

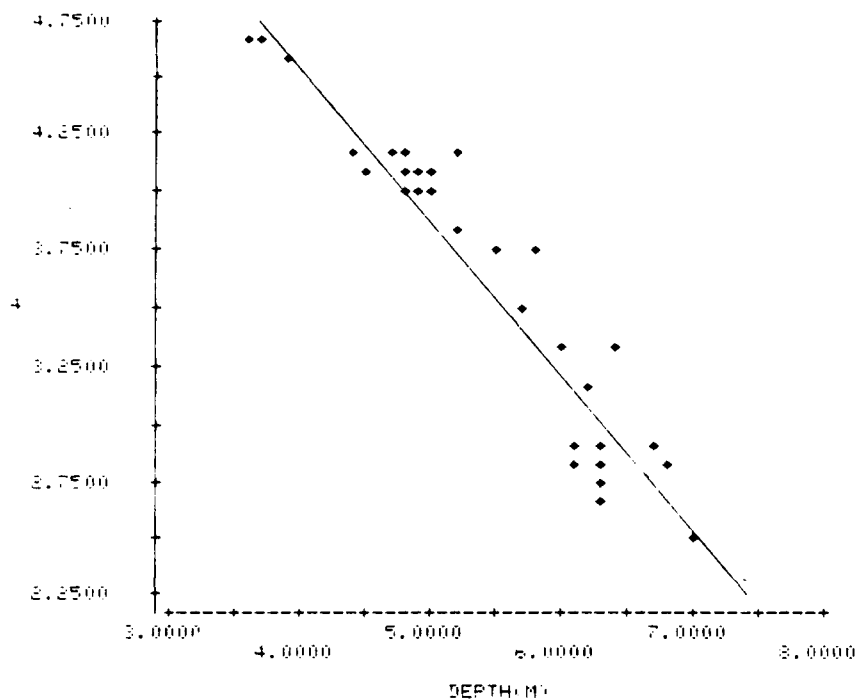


Figure 6c. Passive signals in band C4 versus depth. Vertical axis is log of bottom-reflected signal. Line indicates least-squares fit. Scatter of measured values is due to differences in bottom reflectance.

TABLE 4. IRRADIANCE ATTENUATION COEFFICIENTS FOR WATER OBTAINED
FROM M-8 SCANNER DATA COLLECTED NEAR NORTH CAT CAY ON 8/12/78

<u>Band</u>	<u>Wavelength (μm)</u>	<u>K_i (m^{-1})</u>	<u>Regression Coefficient (r)</u>
C9	.48-.52	.093	0.77
C8	.50-.54	.108	0.81
C7	.52-.57	.114	0.82
C6	.55-.60	.146	0.90
C5	.58-.64	.203	0.92
C4	.62-.70	.335	0.95

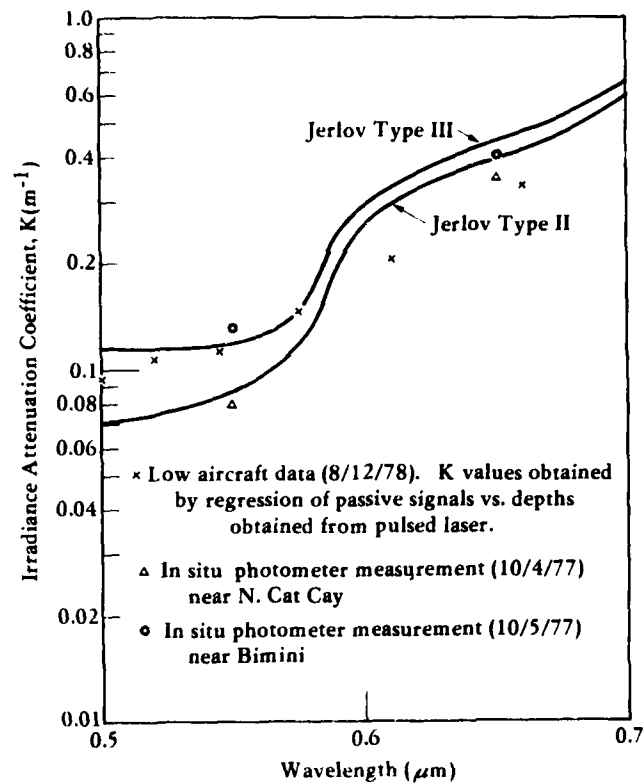


Figure 7. Comparison of irradiance attenuation coefficients obtained from M-8 scanner data with values measured in situ and coefficients tabulated by Jerlov [4].

The second type of information which can be obtained from the pulsed laser data is the effective attenuation coefficient for the laser beam. This coefficient may be obtained by a regression analysis of the amplitude of the bottom-reflected pulse against the depth. A plot of the natural logarithm of this amplitude versus depth is shown in Figure 8 for a set of sand points south of North Cat Cay. The slope of the regression line for this data is -0.618 , with an r -value of 0.94 . Thus, the effective attenuation coefficient is 0.309 m^{-1} at the laser wavelength of $0.52 \text{ }\mu\text{m}$. No in situ measurements of the beam attenuation coefficients were made, but it is interesting to note that the empirical relationship reported by Shannon [5] between the beam attenuation coefficient (α) and the irradiance attenuation coefficient (K) at $0.535 \text{ }\mu\text{m}$,

$$K \approx 0.2\alpha + 0.04 \text{ m}^{-1} \quad (6)$$

holds quite accurately for the laser attenuation coefficient and the irradiance attenuation coefficient obtained from the passive band C3 (0.05 - $0.54 \text{ }\mu\text{m}$). Substituting the value 0.309 m^{-1} for α in equation (6) yields the value 0.102 m^{-1} for K , which compares quite closely to the value of 0.108 m^{-1} in table 4 for band C3.

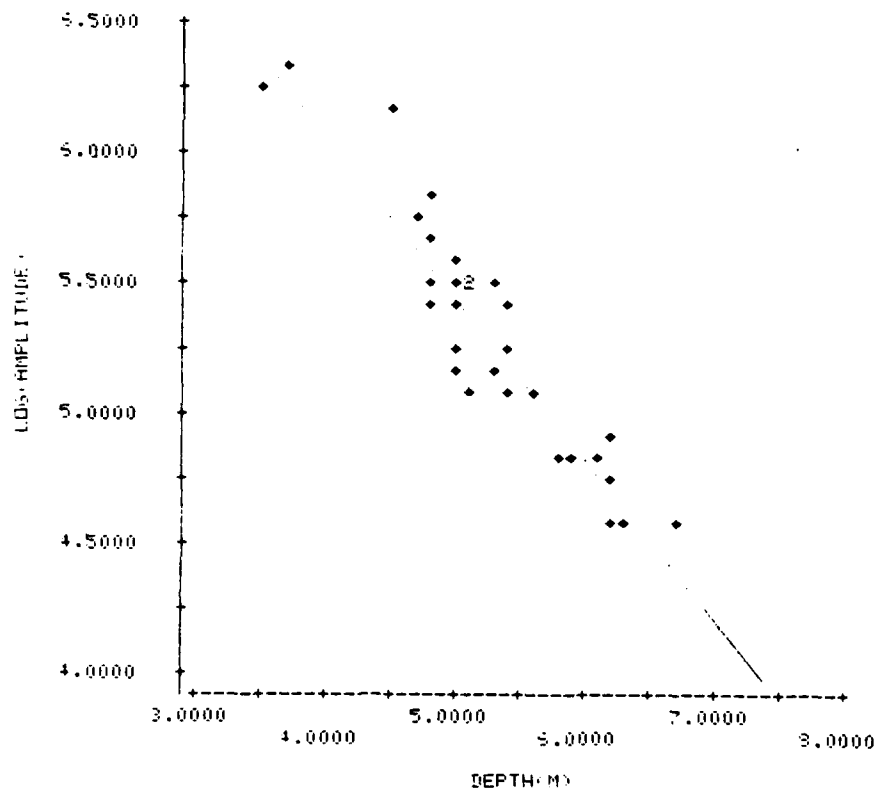


Figure 8. Amplitude of bottom-reflected laser pulse versus depth. Line indicates least-squares fit to data.

3.0

BOTTOM FEATURES

3.1 DATA ANALYSIS

The reflectance of shallow water areas to solar illumination is a function of the water depth, the water optical properties, and the bottom reflectance. Assuming the water optical properties to be uniform over a given scene area, the signals recorded by a multispectral scanner system may be combined to obtain information on the bottom reflectance without knowledge of the water depth. The method of extracting this information has been described in previous reports [1,2] and has been evaluated for a test site in relatively turbid water [6] using low altitude aircraft MSS data. An evaluation of the same algorithm in clear oceanic water is described in this report using higher altitude aircraft and Landsat data. The analysis of the MSS data is described in this section, and an evaluation of the results by comparison with field observations is presented in the following section.

The basis for the bottom reflectance algorithm is the behavior of the X_i variables discussed in Section 2.1 and illustrated in Figure 1: namely, that for a given bottom reflectance the data points fall along a straight line whose slope is K_i/K_j , while changes in bottom cause a displacement perpendicular to this line. We may therefore define the variable

$$Y_i = \frac{K_j \ln(L_i - L_{si}) - K_i \ln(L_j - L_{sj})}{\sqrt{K_i^2 + K_j^2}} \quad (7)$$

as a measure of this displacement. Note that equation (7) can be re-written so that it involves only the ratio of attenuation coefficients K_i/K_j , which can be obtained by the procedure described in

section 2.1. Under the assumption that the bottom-reflected radiance ($L_i - L_{si}$) is proportional to the bottom reflectance and exponentially dependent on the water depth, the variable Y_i is independent of the water depth and is related to the bottom reflectance as follows:

$$Y_i = Y_{io} + \frac{K_j \ln r_i - K_i \ln r_j}{\sqrt{K_i^2 + K_j^2}} \quad (8)$$

where r_i is the bottom reflectance in band i and Y_{io} is a constant for fixed illumination and atmospheric conditions.

This procedure can be implemented as an MSS data processing algorithm by calculating the variable Y_i at each point in the scene and using this variable as a depth-invariant index of the bottom type. If only two wavelength bands are involved, this variable would represent the end-point of the processing and could be used, for example, to generate a film image on which the density is proportional to the Y_i value. This image could then be interpreted as a map of the bottom reflectance, in which the effects of water depth variations have been removed. Alternatively, this index could be calculated for a number of band pairs and the resulting set of Y_i values could be used as inputs to a multispectral pattern recognition or classification routine in order to categorize the bottom into a set of discrete classes. In that case, the algorithm could be viewed as a preprocessing step to remove the effects of water depth variations, analogous to existing routines for removing atmospheric effects or scan angle variations.

The aircraft data set described in Section 2.1 was processed using this algorithm in order to evaluate the performance of the algorithm under clear-water conditions. After preparing the data set as described in section 2.1 and determining the ratios of attenuation

coefficients for each band pair, the next step is to choose a set of wavelength bands for processing.

The choice of wavelength bands to be used in the bottom reflectance processing is determined by a trade-off between depth of penetration and sensitivity to reflectance changes. For a small (Δr) in the bottom reflectance (r), assuming the fractional change to be the same in both bands, the change in the bottom index is

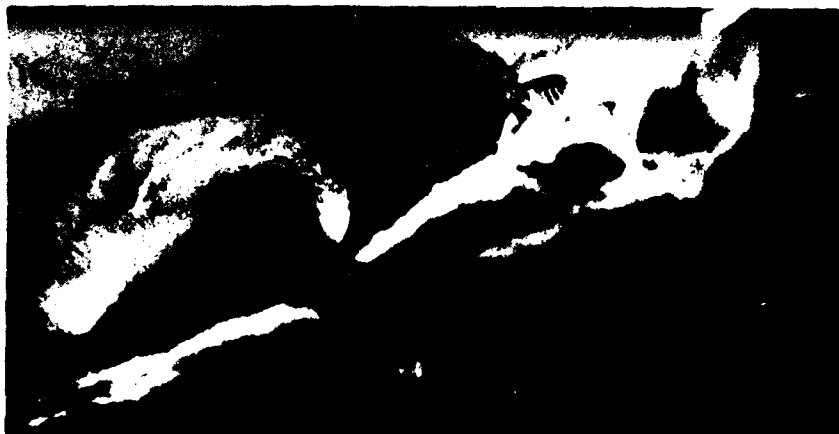
$$\Delta Y_i = \frac{K_j - K_i}{\sqrt{K_i^2 + K_j^2}} \frac{\Delta r}{r} \quad (9)$$

Thus, the sensitivity to changes in bottom reflectance is largest for bands having the greatest difference in attenuation coefficients. On the other hand, this difference cannot be indefinitely increased without simultaneously decreasing the depth of penetration (approximately $1/K_j$, if K_j is the larger of the attenuation coefficients). Obviously one band should be chosen to minimize K_i , but the other band must be chosen to achieve a compromise between sensitivity and penetration depth. In the data set under consideration, data quality is also a consideration, since the gain settings of some bands were either higher or lower than optimal. For this reason, band C7 was chosen instead of C8 or C9 on the basis of data quality, although these bands had a slightly smaller attenuation, and band C5 was chosen to balance sensitivity against penetration depth.

Having selected the wavelength bands and determined the ratio of water attenuation coefficients for these bands (c.f. Table 2), the bottom-type index was calculated point-by-point for the scene, and an output image was generated from this index. This image is shown in Figure 9, along with the single-band images for bands C7 and C5. Exposed land areas were edited out using the thermal band, and appear



a. Band C7 (.52-.57 μm)



b. Band C5 (.58-.64 μm)



c. Bottom-reflectance map

Figure 9. Images generated from M-8 aircraft scanner data collected on 12 August 1978 at 3.3 km altitude.

as white in these images. The image brightness in Figure 9c may be interpreted as being approximately proportional to the bottom reflectance (neglecting spectral variations in the reflectance), whereas Figures 9a and 9b are influenced by water depth as well as bottom reflectance. Thus, the darker areas on the left side of the single-band images appear as a brighter tone on the bottom image, since these areas are characterized by a large water depth but a fairly highly reflecting bottom. The dark areas near the islands, on the other hand, appear dark on all the images since they correspond to vegetated areas in shallow water. A further evaluation of these results is presented in section 3.2 of this report.

Next, the Landsat data set (frame 2293-14385) was processed in order to evaluate the utility of the bottom reflectance algorithm as applied to data collected from satellite altitudes, at a coarser spatial resolution. Using the deep-water signals and the ratio of attenuation coefficients determined from the analysis described in section 2.1 the bottom-type index (Y_1) was generated point-by-point for the portion of the frame covering the North Cat Cay test site. The image generated from this index is shown in Figure 10, along with the raw data images for MSS 4 and MSS 5. Land was edited out from these images using the signal in MSS 7 (0.8-1.1 μ m) to discriminate between land and water. A small geometric correction was also applied to this data to correct for image skew due to earth rotation effects.

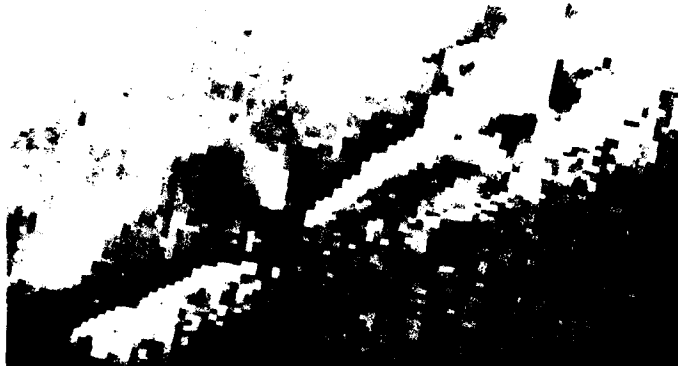
Making allowances for the difference in spatial resolution, the Landsat bottom map (Figure 10c) is similar to the aircraft bottom map (Figure 9c) in the shallow-water areas near the islands. In deeper water, on the left side of the scene, the Landsat image is generally noisier and has a higher proportion of dark bottom classifications. This is probably due to the relatively higher water attenuation in MSS5 than in band C5 of the aircraft scanner, and the lower signal-to-



a. MSS4 (.50-.60 μm)



b. MSS5 (.60-.70 μm)



c. Bottom-reflectance map

Figure 10. Images generated from Landsat data, frame 2993-14385 (11 October 1977).

noise ratio of the Landsat scanner. There is also a dark spot in the Landsat image south of North Cat Cay, which is caused by the shadow of a small cloud appearing in the lower right corner of the image. Further evaluation is presented in the following section.

3.2 EVALUATION OF RESULTS

The results of the bottom reflectance mapping algorithm were evaluated by direct observations of the bottom conditions at nine stations within the test site. The locations of the stations are shown in Figure 2, and a summary of the observations is contained in Table 5. The bottom reflectances indicated in Table 5 were obtained by analyzing underwater photographs of the bottom, examples of which are shown in Figure 11. Each photograph included a calibrated gray scale having reflectances of 1.8 percent, 8.6 percent, and 28.7 percent for each panel. The photographs were scanned with a microdensitometer to determine the film density for each gray panel and for the bottom. The gray panel readings were used to obtain a relationship between film density and panel reflectance, which was then used to infer the bottom reflectance. Adequate sampling of the bottom reflectance is a problem, since the field of view of the underwater camera is much smaller than the resolution of the remote sensing data. In order to alleviate this problem, attempts were made to locate the stations in relatively homogeneous areas, with the exception of stations A-1 and B-3 which were located at the boundaries of vegetated areas.

After processing the aircraft and Landsat data, the coordinates of each station were determined by overlaying a map (Figure 2) on the processed image. The bottom-type indices (the Y-values) were extracted from the digital data at each station, and are shown in Table 6 and Figure 12. For the aircraft data, the Y-value predicts the bottom reflectance with a standard error of 1.8 reflectance units. For the

TABLE 5
SUMMARY OF BOTTOM OBSERVATIONS AT TEST LOCATIONS

<u>Station</u>	<u>Depth (m)</u>	<u>Reflectance (%)</u>	<u>Description</u>
A-1	3	16.0	boundary of vegetated area
A-2	3	5.0	Thalassia bed
A-3	3	32.0	white carbonate sand
B-1	5	16.5	hard, non-vegetated bottom
B-2	4	30.0	white carbonate sand
B-3	3	12.5	boundary of vegetated area
B-4	4	5.0	Thalassia bed
C-1	3	35.0	white carbonate sand
C-2	4	3.0	Thalassia bed



Figure 11a. Underwater photograph at station B-1 (hard, non-vegetated bottom).



Figure 11b. Underwater photograph at station B-2 (white carbonate sand).



Figure 11c. Underwater photograph at station C-2 (*Thalassia* bed).

TABLE 6
BOTTOM-TYPE INDICES CALCULATED FROM
AIRCRAFT AND LANDSAT DATA AT TEST LOCATIONS

Station	<u>Aircraft Data</u>			<u>Landsat Data</u>		
	<u>C7</u>	<u>C5</u>	<u>Y₁</u>	<u>MSS4</u>	<u>MSS5</u>	<u>Y₁</u>
A-1	161	162	2.11	96	35	3.26
A-2	77	77	1.53	59	23	2.48
A-3	248	237	2.40	109	27	3.60
B-1	120	89	2.14	87	22	3.41
B-2	192	150	2.37	112	25	3.70
B-3	102	106	1.77	93	26	3.38
B-4	73	72	1.48	57	22	2.42
C-1	254	224	2.45	127	34	3.70
C-2	69	69	1.39	59	22	2.52
15-m	29.8	48.1	2.22	54.4	17.7	2.83

Values tabulated under C7, C5, MSS4, and MSS5 are signal values (in digital counts). Y₁ is bottom-type index calculated from equation (7).

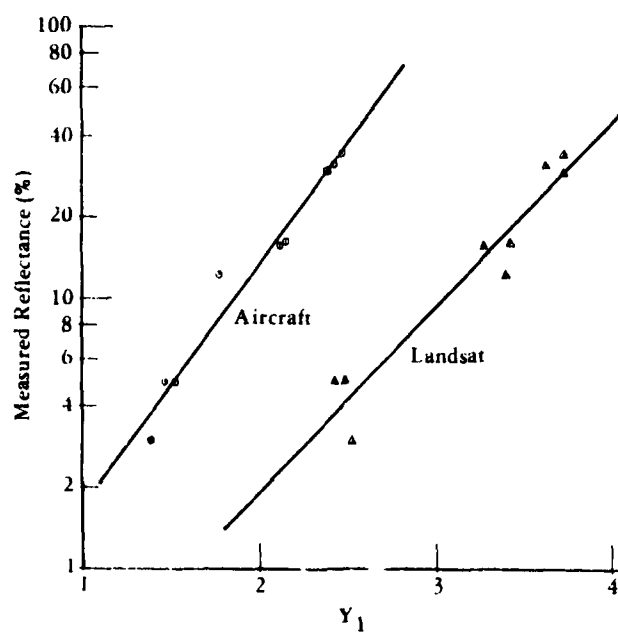


Figure 12. Measured Bottom Reflectance Versus Y_1 Value from Aircraft and Landsat Data.

Landsat data the standard error is 3.6 reflectance units for the nine measurements. It may be noted that over the range of depths for which bottom reflectance measurements were made, the single-band radiances are fairly good predictors of the bottom reflectance. This is not expected to be true over a wider range of depths, however, since water attenuation effects would cause a larger variation in the observed radiance than bottom reflectance effects. To test the expectation, an area further offshore was selected (see box in Figure 2) which has a depth of approximately 15 meters and a bottom composed of white coral and sand, according to DMA chart No. 26324. Color aerial photography seems to indicate a bottom similar to that at station B-1, although the difference in depth makes the bottom type somewhat difficult to judge. Single-band data values and Y-values were extracted from both the aircraft and Landsat data sets for this area, and are shown in Table 6. Using a regression fit between the single-band data values and the bottom reflectances at the nine stations, the bottom reflectances predicted by C5 and C7 are 2.8 percent and 6.7 percent, respectively, both of which are much too low. The bottom reflectance predicted by the Y-value for the aircraft data is 21.8 percent, which is probably quite close to the correct value judging from the reflectance at B-1. For the Landsat data the MSS-5 radiance is not significantly above the deep-water radiance, so the bottom reflectance cannot be reliably calculated. The Y-value indicated in Table 6 for the Landsat data implies a reflectance of 7.4 percent, which is in fact much too low.

4.0

RADIATIVE TRANSFER MODELING

4.1 WATER MODELING

A radiative transfer model consisting of a modification of the QSS approximation [2,7] was used for the development and theoretical evaluation of the bottom reflectance algorithm. This model has the virtue of computational efficiency and gives acceptably accurate results for most cases of interest for passive remote sensing, although it is known to break down in highly turbid water. The assumptions of the model are that the water properties are vertically homogeneous, that the water and bottom are horizontally uniform, and that the source of illumination is constant and horizontally uniform. These assumptions are not overly restrictive for modeling the passive case, but are not applicable to the active (pulsed-laser) case.

In anticipation of the need for modeling the response of the active scanner, a Monte Carlo simulation model is being developed. The advantage of this model is that it is "exact" in the sense that results can be obtained to any required degree of accuracy given enough computer time, and that it can be modified to simulate complex geometries and boundary conditions. It can also generate time-dependent solutions and account for narrow beam illumination conditions. The disadvantage of the Monte Carlo method is that a large amount of computer time may be required to generate accurate results for some situations. For this reason, efforts are also being made to develop approximate analytical models which are applicable to the active case. The Monte Carlo program will be used to test the accuracy and range of validity of these models.

The method used in the Monte Carlo model is to "follow" a large number of individual photons as they pass through the medium. The path of each photon is simulated by choosing the path lengths and scattering angles from the appropriate distribution functions. When the photon encounters a boundary, the appropriate boundary conditions are applied, or if the

photon emerges from the medium the relevant properties (such as angle, position, and/or time) of the emerging photon are recorded. The number of interactions undergone by the photon before emerging is also recorded. Since the probability of scattering (as opposed to absorption) at each interaction is given by the single-scattering albedo, ω_0 , the emerging photon is assigned a statistical weight $(\omega_0)^n$ where n is the number of interactions undergone before emerging. Thus, the same set of statistics may be used to calculate the reflectance for a number of different values of ω_0 . Other techniques are possible to increase computational efficiency, but generally at the cost of reducing the flexibility of the model.

A FORTRAN source listing for the basic Monte Carlo model is given in Appendix A. This version records only the polar angle of the emerging photons and considers only one boundary, at $Z=0$. Thus, the result of this program is the azimuthally averaged reflectance for a semi-infinite medium. Modifications for the pulsed laser operating in shallow water would be to record also the position and time of the emerging photons and to consider a second boundary at the ocean floor. Modifications could also be made to include a vertical stratification of the water properties.

4.2 ATMOSPHERIC MODELING

The primary difference between the radiative transfer problems in water and in the atmosphere is the relative amount of absorption. In water, the single-scattering albedo ω_0 (defined as the ratio of scattering to total attenuation) is typically around 0.5 and rarely exceeds 0.9 except in highly turbid water. In the atmosphere, on the other hand, absorption is negligible in the visible region of the spectrum and the value of ω_0 is 1.0 for practical purposes. Because the QSS model is known to break down as $\omega_0 \rightarrow 1$, at least for large optical thickness, a different model has been used in the past for atmospheric

calculations. The double-delta model developed by Turner [8] is in relatively wide use for this application. However, a problem has been recently reported [9] in that the reflectance predicted by this model is much too large in the anti-solar direction. Although this problem was reported for the case of optically thick clouds, it appears to exist also for the path radiance in a relatively thin atmosphere. As a result, a re-examination of various models has been conducted with reference to their performance in the conservative scattering use ($\omega_0=1$). The QSS model was included in this comparison and found to yield results at least as good as the Turner model in most cases, although it does break down for large optical thicknesses. A new model was developed during the course of this study which is slightly superior to both the QSS and double-delta model for predicting backscattered radiances, particularly for optically thick media.

For the case of direct incident irradiance $\mu_0 E_0$ on a plane-parallel atmosphere, the transfer equation may be written [10] as

$$\mu \frac{dL}{d\tau} = L(\tau, \mu, \phi) - \frac{\omega_0}{4\pi} \int_{-1}^1 \int_0^{2\pi} p(\mu, \phi; \mu', \phi') L(\tau, \mu', \phi') d\mu' d\phi' - \frac{\omega_0 E_0}{4\pi} e^{-\frac{\tau}{\mu_0}} p(\mu, \phi; -\mu_0, \phi_0) \quad (10)$$

where $L(\tau, \mu, \phi)$ represents the diffuse radiance which has arisen from one or more scattering processes. The Neumann solution is obtained by solving this equation without the integral term (i.e., setting $L=0$ in the integral) to obtain a first-order radiance $L^{(1)}$, then substituting the first-order radiance in the integral term and solving for the second order radiance $L^{(2)}$, etc. The n^{th} order radiance $L^{(n)}$ in this series has the physical interpretation of the radiance arising from n scatterings of the

beam. The difficulty of this method is that analytical solutions are not obtainable beyond the first order, so that numerical integration is necessary, and that the series converges very slowly for thick layers as $\omega_0 \gg 1$.

In the QSS model, the approximate phase function

$$p^*(\mu, \phi; \mu', \phi') = \begin{cases} 4\pi F \delta(\mu - \mu') \delta(\phi - \phi') & \mu\mu' > 0 \\ p(\mu, \phi; \mu', \phi') & \mu\mu' \leq 0 \end{cases} \quad (11)$$

is substituted for the actual phase function $p(\mu, \phi; \mu', \phi')$ in equation (10), resulting in the set of equations

$$\begin{aligned} \mu \frac{dL}{d\tau} = (1 - \omega_0 F)L - \frac{\omega_0}{4\pi} \int_0^{2\pi} \int_0^1 p(\mu, \phi; \mu', \phi') L(\tau, \mu', \phi') d\mu' d\phi' \\ - \omega_0 F E_0 e^{-\pi/\mu_0} \delta(\mu + \mu_0) \delta(\phi - \phi_0) \end{aligned} \quad (12)$$

for $\mu > 0$, and

$$\begin{aligned} \mu \frac{dL}{d\tau} = (1 - \omega_0 F)L - \frac{\omega_0}{4\pi} \int_0^{2\pi} \int_{-1}^0 p(\mu, \phi; \mu', \phi') L(\tau, \mu', \phi') d\mu' d\phi' \\ - \frac{\omega_0 E_0}{4\pi} e^{-\pi/\mu_0} p(\mu, \phi; -\mu_0, \phi_0) \end{aligned} \quad (13)$$

for $\mu < 0$.

Equation (12) may be solved in the single-scattering approximation (by neglecting the integral term) to yield

$$L^{(1)}(\tau, \mu, \phi) = E_0 \left[e^{-(1-\omega_0 F)\tau/\mu_0} - e^{-\tau/\mu_0} \right] \delta(\mu + \mu_0) \delta(\phi - \phi_0) \quad (14)$$

for $\mu=0$. Substituting this in equation (13) and solving for L , we obtain

$$L^{(1)}(\tau, \mu, \phi) = \frac{\omega_o' \mu_o E_o}{4\pi(\mu + \mu_o)} e^{-\tau'/\mu_o} \left[1 - e^{-(\tau' - \tau'_o)(1/\mu + 1/\mu_o)} \right] p(\mu, \phi; -\mu_o, \phi_o) \quad (15)$$

for $\mu \geq 0$, where $\tau' = (1 - \omega_o F)\tau$ and $\omega_o' = \omega_o / (1 - \omega_o F)$. Gordon [7] showed that this approximation yields a hemispherical reflectance which agrees with an exact calculation to within 0.5 percent for $\omega_o \leq 0.6$ and to within about 12 percent for $\omega_o \leq 0.85$ for the semi-infinite case ($\tau = \infty$). It does not predict the forward-scattered radiance, however, and the errors in the back-scattered radiance increase as $\omega_o \rightarrow 1$.

In order to test the QSS model for the atmospheric case (i.e., $\omega_o = 1$, $\tau_o = \infty$), calculations of $L^{(1)}(0, \mu, \phi)$ from equation (15) were compared with exact results calculated by Hansen [11] using the doubling method. The phase function used for this comparison is shown in Figure 13. The reflection function

$$R(\tau; \mu, \phi; \mu_o, \phi_o) = \frac{\pi}{E_o} L(0, \mu, \phi) \quad (16)$$

is plotted versus μ for the case $\mu_o = 1$ (normal incidence) in Figure 14(a), and for the case $\mu_o = 0.5$ in Figure 14(b). Fairly good agreement is noted for the case of normal incidence with $\tau_o = 1$, but large errors exist for the other cases. More accurate results could probably be obtained by doing a second iteration: i.e., by substituting equations (14) and (15) into the integral term of the transfer equation (10) and solving for $L^{(2)}(\tau, \mu, \phi)$. This would involve a numerical integration over μ' and τ' , however, which detracts from the simplicity of the model.

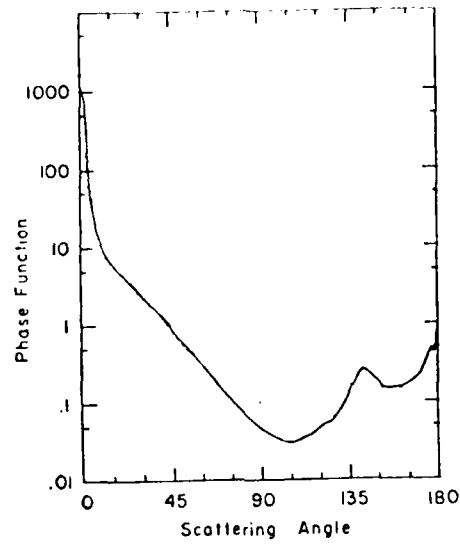
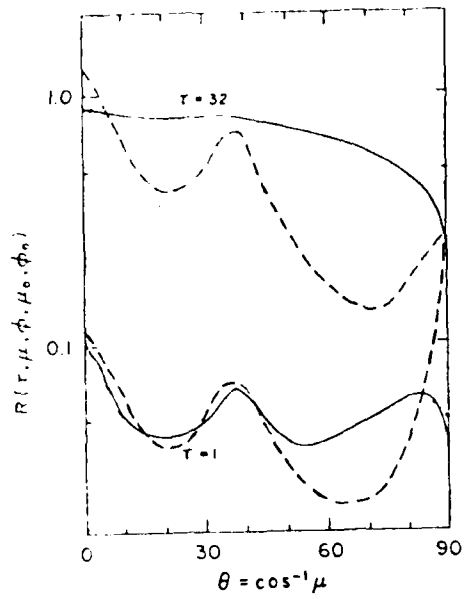
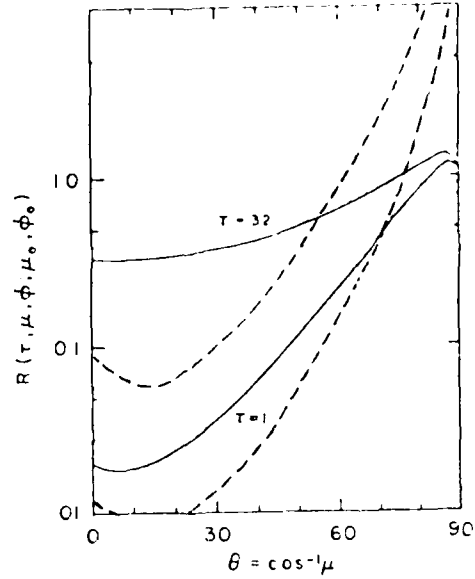


Figure 13. Phase function used by Hansen [11] for reflectance calculations.



(a) $\theta_0 = 0^\circ$



(b) $\theta_0 = 60^\circ, \phi - \phi_0 = 0^\circ$

Figure 14. Comparison of QSS model with exact calculations by Hansen [11]. Dashed line indicates QSS model.

The approach taken by Turner [8] in the double-delta model is to use the approximate phase function

$$p'(\mu, \phi; \mu', \phi') = 4\pi F \delta(\mu - \mu') \delta(\phi - \phi') + 4\pi B \delta(\mu + \mu') \delta(\phi - \phi' + \pi) \quad (17)$$

in the transfer equation (10) and to solve for the first-order radiance

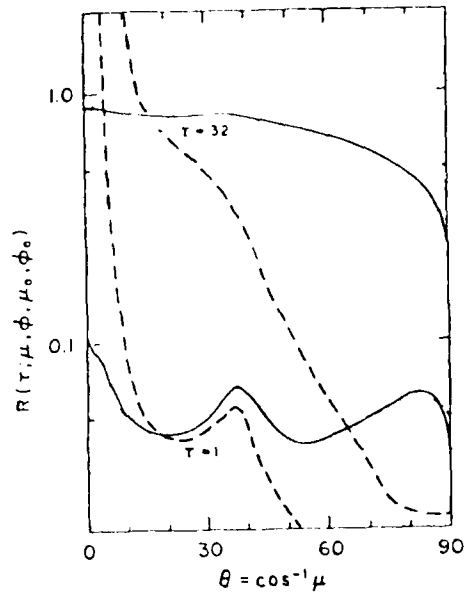
$$L^{(1)}(\tau, \mu, \phi) = \frac{1}{\mu_0} \left[E_-(\tau) \delta(\mu + \mu_0) \delta(\phi - \phi_0) + E_+(\tau) \delta(\mu - \mu_0) \delta(\phi - \phi_0 + \pi) \right] \quad (18)$$

Solutions for $E_-(\tau)$ and $E_+(\tau)$ have been given by Turner [8] for $\omega_0 = 1$ and by Zachor et al [12] for $\omega_0 \leq 1$. Substituting equation (18) into the integral term of the transfer equation (10) yields a second-order solution which is the one generally referred to as the double-delta model. Again, further iterations could be done, but would require numerical integrations and a more complex computer code.

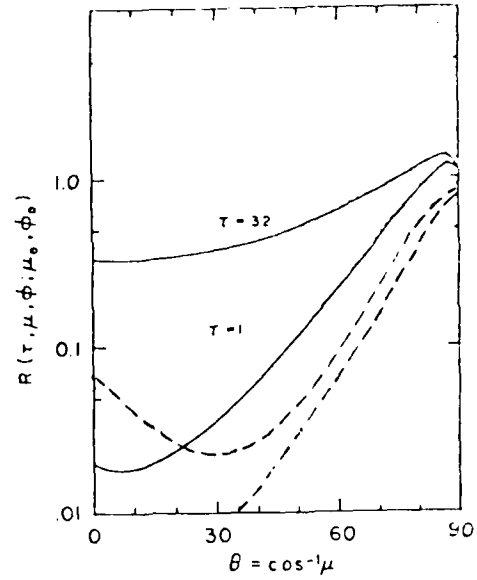
A comparison of the reflection function for the double-delta model with Hansen's exact calculations is shown in Figures 15(a) and 15(b). Figure 15(a) shows the overestimate of the radiance in the anti-solar direction ($\theta = 0^\circ$), which increases with increasing optical thickness. (This effect is also present for optical thicknesses less than one.) Figure 15(b) does not include the anti-solar direction, but shows that the double-delta model generally underestimates the radiance in other directions.

This analysis of the limitations of the QSS and double-delta model suggests several other possible approaches to obtaining an approximate solution of the transfer equation. One such approach is to use a phase function of the form

$$p'(\mu, \phi; \mu', \phi') = 4\pi g \delta(\mu - \mu') \delta(\phi - \phi') + 1 - g \quad (19)$$



(a) $\theta_0 = 0^\circ$



(b) $\theta_0 = 60^\circ$, $\phi - \phi_0 = 0^\circ$

Figure 15. Comparison of double-delta model with exact calculations by Hansen [11]. Dashed line indicates double-delta model.

in order to obtain a first-order solution. If an approximate first-order solution is obtained in the form

$$L^{(1)}(\tau, \mu, \phi) = E_-(\tau) \delta(\mu + \mu_0) \delta(\phi - \phi_0) + L_0(\tau) + \mu L_1(\tau) \quad (20)$$

using the Eddington approximation, this solution can then be substituted back into the integral term of the transfer equation in order to obtain a second-order solution in closed form.

Substituting the phase function (19) into the transfer equation one readily obtains

$$E_-(\tau) = E_0 \left[e^{\frac{-(1-\omega_0 g)\tau}{\mu_0}} - e^{-\tau/\mu_0} \right] \quad (21)$$

In the Eddington approximation, the terms $L_0(\tau)$ and $L_1(\tau)$ are obtained by substituting (20) into the transfer equation and taking the first two moments of this equation (i.e., integrating over μ , then multiplying by μ and integrating). The result is the set of equations

$$\frac{dL_0}{d\tau} = L_1 \quad (22)$$

$$\frac{dL_1}{d\tau} = 3(1-\omega_0 g)L_0 - \frac{3\omega_0 g}{4\pi} E_0 e^{-\tau/\mu_0}$$

where $\tau' = (1-\omega_0 g)\tau$ and $\omega_0 g = \frac{\omega_0(1-g)}{1-\omega_0 g}$. For the case $\omega_0 = \omega_0' = 1$, this set of equations has the solution

$$L_0(\tau) = \frac{3\mu_0 E_0}{4\pi} \left[\mu_0 (1 - e^{-\tau'/\mu_0}) + C\tau' + \frac{2}{3}(1+C) \right] \quad (24)$$

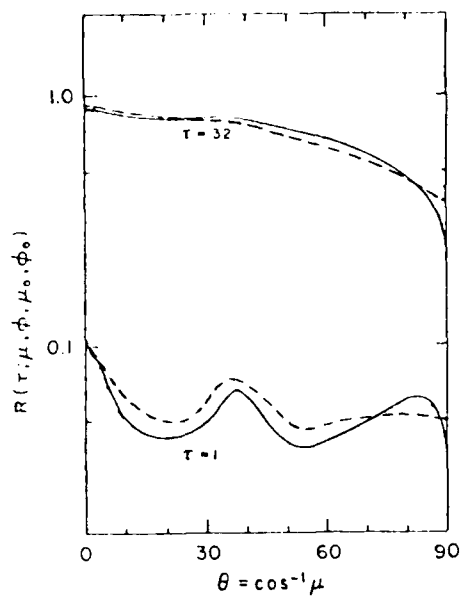
$$L_1(\tau) = \frac{3\mu_0 E_0}{4\pi} \left[e^{-\tau'/\mu_0} + C \right] \quad (25)$$

$$\text{where } C = \frac{\left(\mu_o - \frac{2}{3}\right) e^{-\tau_o/\mu_o} - \left(\mu_o + \frac{2}{3}\right)}{\tau_o + \frac{4}{3}} \quad (26)$$

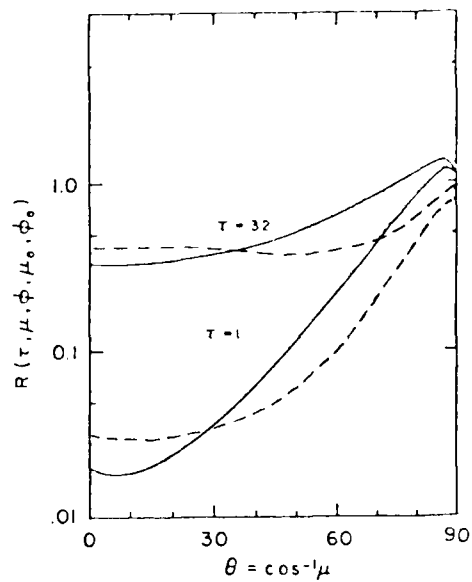
This first-order solution can then be substituted back into the transfer equation, and a second-order solution obtained. The solution is somewhat more complicated than the QSS solution but is not untractable. At $\tau=0$, the reflected radiance ($\mu>0$) can be written as

$$\begin{aligned} I^{(2)}(0, \mu, \phi) = & \frac{\mu_o E_o}{4\pi [\mu_o + (1-g)\mu]} \left[p(\mu, \phi; -\mu_o, \phi_o) + 3\mu_o (\mu g - \mu_o) \right] \\ & \cdot \left\{ \frac{1}{1-e} - \left[\frac{1}{\mu + (1-g)1/\mu_o} \right] \tau_o \right\} \\ & + \frac{3\mu_o E_o}{4\pi} \left\{ \left[\mu_o + \frac{2}{3} + \left(\mu + \frac{2}{3} \right) C \right] (1-e^{-\tau_o/\mu}) - C(1-g)\tau_o e^{-\tau_o/\mu} \right\} \end{aligned} \quad (27)$$

A comparison of this result with Hansen's exact calculation is shown in Figures 16(a) and 16(b). The agreement is generally better than that for either the QSS or double-delta models, although **the results obviously are not exact**. A FORTRAN source listing for the computer program used to calculate these results is given in Appendix B.



(a) $\theta_0 = 0^\circ$



(b) $\theta_0 = 60^\circ$, $\phi - \phi_0 = 0^\circ$

Figure 16. Comparison of iterated Eddington model with exact results by Hansen [11]. Dashed line indicates iterated Eddington model.

5.0

CONCLUSIONS AND RECOMMENDATIONS

Information can be obtained from active and/or passive multispectral scanner data on both bottom reflectance and water attenuation parameters in shallow water, provided that the assumption of uniform water properties can be made. This information has potential applications to studies of marine biology and geology, as well as to the remote measurement of water depth, as outlined below. The water parameters which can be obtained from passive-only data are the ratios of the irradiance attenuation coefficients in the wavelength bands used. Using active (lidar) techniques in conjunction with the passive data, the absolute values of the irradiance attenuation coefficients can be obtained as well. These parameters are determined for the entire scene, while the bottom reflectance is calculated at each point in the scene.

The information extraction algorithms described in this report are relevant to remote bathymetry studies in several respects. The water parameter information can be used to estimate the maximum depth which can be mapped by remote sensing techniques, and can also supply input parameters needed by these techniques. The bottom reflectance information can likewise be used to supply input parameters and to make corrections for bottom color variations in the water depth calculations.

It does not yet appear to be possible to devise a computer algorithm for distinguishing water parameter variations from bottom reflectance or water depth variations, although it is frequently possible for a trained photo-interpreter to make this judgement, probably on the basis of spatial or textural differences. The assumption of uniform water properties appears to be much more frequently valid than the assumption of uniform bottom reflectances. However, more in situ water measurements are needed to assess the spatial variability of the water attenuation coefficient and to directly verify the results of the water attenuation extraction algorithms.

Very little direct information is available on the spatial variation of the irradiance attenuation coefficient. This lack of information is due in large part to the difficulty of obtaining irradiance attenuation data in shallow water. The conventional method of obtaining the irradiance attenuation coefficient is to make a series of measurements of the irradiance at different depths, using a submersible photometer. This method is difficult to apply in shallow water because the problem of shadowing the photometer is more severe and because the range of depths over which measurements can be made is more limited. Beam attenuation measurements are easier to make in shallow water, because these measurements can be made with transmissometers that use an internal light source and require a shorter path length. However, these measurements are not easily related to the irradiance attenuation coefficient, which is the relevant parameter for remote sensing, unless independent measurements of the scattering function are made simultaneously. What is needed, therefore, is a means of making rapid measurements of both the beam attenuation coefficient (μ) and the volume scattering function $\beta(\theta)$. The irradiance attenuation coefficient can be obtained from these measurements by integrating the volume scattering function over the forward hemisphere and subtracting this quantity from the beam attenuation coefficient.

Other areas of research that should be pursued include the extraction of water optical properties using the volume-scattered return from the pulsed laser, and an examination of surface effects. A modeling effort could be undertaken to determine what water parameter information can be extracted from the shape of the returned laser pulse. The results could be initially tested using existing pulsed laser data from the Bahamas, Puerto Rico, or Florida. Definitive testing would require the acquisition of a data set with simultaneous in situ water measurements, however.

Surface reflectance and transmittance effects also deserve further examination. These effects are important for several reasons. First, in the visible region, they represent a source of noise or interference with the subsurface-reflected light for most passive remote sensing applications,

including bathymetry. A better understanding of surface effects would thus aid in the development of more accurate information extraction techniques. Secondly, active systems (such as lidar bathymetry devices) require that a recognizable surface-reflected signal be recorded, and it is important to design and operate these systems so that this condition is met. Thirdly, useful information on sea state and wave parameters may be contained in the surface-reflected signals and improved techniques are necessary to extract this information.

APPENDIX A: FORTRAN Code for Monte Carlo Model

```

1  C MONTE CARLO RADIATIVE TRANSFER PROGRAM
2  C NAMELIST /INPUT/ X0,Y0,Z0,THETA,PHI,NPMAX,NIMAX,IS,NR,P,TH,NTH,
3  C   I NAI,W0,NW0
4  C (X0,Y0,Z0)=INITIAL POSITION OF PHOTON
5  C (THETA,PHI)=INITIAL DIRECTION OF PHOTON (DEGREES)
6  C NPMAX=MAXIMUM NUMBER OF PHOTONS CONSIDERED
7  C NIMAX=MAXIMUM NUMBER OF INTERACTIONS CONSIDERED(<50)
8  C IS=INITIAL SEED FOR RANDOM NUMBER GENERATOR
9  C NR=INDEX OF REFRACTION OF MEDIUM
10 C P(I)=SCATTERING PHASE FUNCTION OF MEDIUM
11 C TH(I)=SCATTERING ANGLE (DEGREES)
12 C NTH=NUMBER OF SCATTERING ANGLES(<30)
13 C NAI=NUMBER OF ANGLE INTERVALS FOR COUNTING EMERGING PHOTONS(<50)
14 C W0(I)=SINGLE-SCATTERING ALBEDO
15 C NW0=NUMBER OF VALUES FOR SINGLE-SCATTERING ALBEDO(<10)
16 C   REAL P(30),TH(30),NR
17 C   INTEGER BIN(50,50),NEP(50)
18 C   REAL R(10),RH(10),RE(10),THR(50),W0(10)
19 C   DATA X0,Y0,Z0/0.,0.,0./
20 C   DATA THETA,PHI/0.,0./
21 C   DATA NPMAX/10000/
22 C   DATA NIMAX/10/
23 C   DATA IS/1/
24 C   DATA NR/1.333/
25 C   DATA P/45.77,5.34,1.58,.294,.120,.0366,.0158,.00915,.00661,.00641,
26 C   1 .00732,.00829,.0107,.0126,.0131,.0134,.0136,13*0./
27 C   DATA TH/1.,5.,10.,20.,30.,45.,60.,75.,90.,105.,120.,135.,150.,
28 C   1 165.,170.,175.,180.,13*0./
29 C   DATA NTH/17/
30 C   DATA NAI/10/
31 C   DATA W0/.1,.2,.3,.4,.5,.6,.7,.8,.9,1.0/
32 C   DATA NW0/9/
33 C   INTEGER*2 ANS/' ',YES/'Y',NO/'N'/
34 C   REAL*8 DASHES/' -----'/
35 C   PI=ACOS(-1.0)
36 C   TWOPI=2.*PI
37 C   DEGRAD=PI/180.
38 C   CALL FCVTHR(1)
39 C   10 WRITE(6,100)
40 C   100 FORMAT('ENTER INPUT PARAMETERS (NAMELIST FORMAT):')
41 C   WRITE(6,INPUT)
42 C   READ(5,INPUT)
43 C   WRITE(7,INPUT)
44 C   C INTEGRATE PHASE FUNCTION
45 C   B=PI*P(P,TH,NTH)
46 C   WRITE(7,102) B
47 C   102 FORMAT('BACKSCATTERING FRACTION =',F7.3)
48 C   C CALCULATE ANGLE INTERVALS AND INITIALIZE BINS TO ZERO
49 C   DO 12 I=1,NAI
50 C     THB(I)=ACOS(SQRT((I-1.)/NAI))/DEGRAD
51 C   DO 12 J=1,NIMAX
52 C     BIN(I,J)=0
53 C   12 CONTINUE
54 C   THR(NAI+1)=0.
55 C   NP=0
56 C   C NP IS NUMBER OF PHOTONS CONSIDERED THUS FAR
57 C   NLP=0
58 C   C NLP IS NUMBER OF PHOTONS NOT EMERGING AFTER NIMAX INTERACTIONS
59 C   ZLP=0.
60 C   20 NP=NP+1

```

```

61      IF(NP.GT.NPMAX) GO TO 60
62      C CONSIDER NEW PHOTON
63      NI=0
64      C RESET INITIAL POSITION AND ANGLE
65      XP=X0
66      YP=Y0
67      ZP=Z0
68      CT=COS(THETA*DEGRAD)
69      ST=SIN(THETA*DEGRAD)
70      CP=COS(PHI*DEGRAD)
71      SP=SIN(PHI*DEGRAD)
72      30 IF(NI.GT.NIMAX) GO TO 50
73      NI=NI+1
74      C CALCULATE DISTANCE D TO NEXT INTERACTION
75      RD=URAND(15)
76      D=-ALOG(RD)
77      C CALCULATE POSITION OF PHOTON AT THIS INTERACTION
78      X=XP+D*ST*CP
79      Y=YP+D*ST*SP
80      Z=ZP+D*CT
81      C CHECK TO SEE IF PHOTON IS STILL IN MEDIUM
82      IF(Z.LT.0.) GO TO 40
83      C CONSIDER NEXT PATH, RESET INITIAL POSITION
84      32 XP=X
85      YP=Y
86      ZP=Z
87      C CALCULATE ROTATION MATRIX FOR PREVIOUS DIRECTION
88      A31=ST*CP
89      A32=ST*SP
90      A33=CT
91      A11=SQRT(1.-A31*A31)
92      A22=A33/A11
93      A23=-A32/A11
94      A12=A31*A23
95      A13=-A31*A22
96      C CALCULATE NEW PHOTON DIRECTION (TP,PP) RELATIVE TO PREVIOUS DIRECTION
97      RT=URAND(15)
98      CTP=PI*RT
99      STP=SQRT(1.-CTP*CTP)
100     RP=URAND(15)
101     PP=TW(PI)*RP
102     CPP=COS(PP)
103     SPP=SIN(PP)
104     C CALCULATE DIRECTION IN ORIGINAL COORDINATE SYSTEM
105     CT=A13*STP+CPP+A23*STP+SPP+A33*CTP
106     ST=SQRT(1.-CT*CT)
107     IF(ST.EQ.0.) GO TO 30
108     CP=(A11*STP+CPP+A31*CTP)/ST
109     SP=(A12*STP+CPP+A22*STP+SPP+A32*CTP)/ST
110     GO TO 30
111     C CHECK TO SEE IF PHOTON IS REFLECTED AT INTERFACE
112     40 STA=NR*ST
113     IF(STA.LT.1.) GO TO 42
114     CT=-CT
115     Z=-Z
116     GO TO 32
117     C ACCUMULATE STATISTICS FOR EMERGING PHOTONS
118     42 NI=NI+1
119     ST2=STA*STA
120     CT2=1.-ST2

```

```

121      NA=NAI*CT2+1
122      BIN(NA,NI)=BIN(NA,NI)+1
123      GO TO 20
124 C   ACCUMULATE STATISTICS FOR "LOST" PHOTONS
125      50 NLP=NLP+1
126      ZLP=ZLP+Z
127      GO TO 20
128 C   PRINT OUT STATISTICS
129      60 WRITE(7,160)
130      160 FORMAT('O ORDER OF',10X,'NUMBER OF '/' INTERACTION',5X,
131      1 'EMERGING PHOTONS')
132      DO 64 J=1,NIMAX
133      NEP(J)=0
134      DO 62 I=1,NAI
135      NEP(J)=NEP(J)+BIN(I,J)
136      62 CONTINUE
137      WRITE(7,162) J,NEP(J)
138      162 FORMAT(17,10X,110)
139      64 CONTINUE
140      ZLP=ZLP/NLP
141      WRITE(7,164) NIMAX,NLP,ZLP
142      164 FORMAT('NUMBER OF PHOTONS NOT EMERGING AFTER',14,' INTERACTIONS =
143      1 ',110,' /' AVERAGE DEPTH OF THESE PHOTONS =',F10.3,' UNITS')
144      WRITE(7,166) (W0(I),I=1,NW0)
145      166 FORMAT('ORIDIRECTIONAL REFLECTANCE (AZIMUTHALLY AVERAGED) X 100 : '
146      1 /'ANGLE INTERVAL',10X,'SINGLE-SCATTERING ALBEDO' /
147      2 ' (DEGREES)',2X,10F7.3)
148      WRITE(7,167) (DASHES,I=1,NW0)
149      167 FORMAT(1X,13(' '),10A7)
150      DO 68 I=1,NAI
151      I1=NAI-I+1
152      I2=NAI-I+2
153      DO 66 K=1,NW0
154      W=1.
155      R(K)=0.
156      DO 66 J=1,NIMAX
157      W=W*W0(K)
158      R(K)=R(K)+100.*W*BIN(I1,J)*NAI/NPMAX/PI
159      66 CONTINUE
160      WRITE(7,168) THB(I2),THB(I1),(R(K),K=1,NW0)
161      168 FORMAT(1X,F9.1,' -',F5.1,1X,10F7.3)
162      68 CONTINUE
163      DO 72 K=1,NW0
164      W=1.
165      RH(K)=0.
166      DO 70 J=1,NIMAX
167      W=W*W0(K)
168      RH(K)=RH(K)+100.*W*NEP(J)/NPMAX
169      70 CONTINUE
170      W=W*W0(K)
171      RE(K)=100.*W*NLP/NPMAX
172      72 CONTINUE
173      WRITE(7,170) (RH(K),K=1,NW0)
174      170 FORMAT('HEMISPHERICAL REFLECTANCE X 100:'/' /'14X,10F7.3)
175      WRITE(7,172) NIMAX,(RE(K),K=1,NW0)
176      172 FORMAT('OMAXIMUM CONTRIBUTION TO HEMISPHERICAL REFLECTANCE' /
177      1 ' FROM PHOTONS SCATTERED MORE THAN',14,' TIMES:'/' /'14X,10F7.3)
178      80 WRITE(6,180)
179      180 FORMAT('OCONTINUE THIS RUN?')
180      READ(5,182) ANS

```

```

181      182 FORMAT(41)
182      IF(ANS.EQ.YFS) GO TO R4
183      IF(ANS.EQ.Nn) GO TO 10
184      GO TO 80
185      84 WRITE(6,184)
186      184 FORMAT('ENTER NUMBER OF ADDITIONAL PHOTONS TO BE CONSIDERED:')
187      READ(5,186) NADP
188      186 FORMAT(110)
189      NPMAX=NPMAX,NADP
190      NP=NP+1
191      ZLP=ZLP+NL P
192      GO TO 20
193      END

```

```

1      FUNCTION PINT(P,TH,NTH)
2      REAL P(30),TH(30),MU(30)
3      REAL A(30),B(30),S(30)
4      DEGRAD=ARCCOS(-1.0)/180.
5      THNP1=360.*DEGRAD
6      DO 10 I=1,NTH
7      MU(I)=COS(TH(I)*DEGRAD)
8      IF(P(I).GT.P(NTH)) NF=I
9      10 CONTINUE
10     C FIT FORWARD LOBE: P=A(I)*(1-MU(I))*B(I) , MU(I)>MU(MU(I+1))
11     NF1=NF-1
12     DO 12 I=1,NF1
13     B(I)=ALOG(P(I)/P(I+1))/ALOG((1.-MU(I))/(1.-MU(I+1)))
14     A(I)=P(I)/(1.-MU(I))*B(I)
15     12 CONTINUE
16     C COMPUTE INTEGRAL S(I) FROM MU=1 TO MU=MU(I)
17     S(I)=P(I)*(1.-MU(I))/(B(I)+1.)
18     DO 14 I=2,NF
19     S(I)=S(I-1)+(P(I)*(1.-MU(I))-P(I-1)*(1.-MU(I-1)))/(B(I-1)+1.)
20     14 CONTINUE
21     C FIT REST OF FUNCTION: P=A(I)+B(I)*MU , MU(I)>MU(MU(I+1))
22     NT1=NTH-1
23     DO 16 I=NF,NT1
24     B(I)=(P(I+1)-P(I))/(MU(I+1)-MU(I))
25     A(I)=P(I)-B(I)*MU(I)
26     16 CONTINUE
27     B(NTH)=B(I)
28     A(NTH)=A(I)
29     C COMPUTE S(I) FOR REST OF FUNCTION
30     NF1=NF+1
31     DO 18 I=NF1,NTH
32     AMU=(MU(I-1)+MU(I))/2.
33     DMU=MU(I-1)-MU(I)
34     S(I)=S(I-1)+(A(I-1)+B(I-1)*AMU)*DMU
35     18 CONTINUE
36     ST=S(I)
37     IF(MU(I).NE.-1.) ST=ST+(A(I)+B(I)*(MU(I)-1.)/2.)*(MU(I)+1.)
38     C COMPUTE BACKSCATTERING FRACTION
39     DO 20 I=1,NTH
40     IF(MU(I)) 22,22,20
41     20 CONTINUE
42     I=1-1
43     IF(I.GE.NF) GO TO 24
44     FS=S(I)+(A(I)-P(I))/(B(I)+1.)
45     GO TO 26

```

```

46      24 FS=S(I)+(A(I)+B(I)*MU(I)/2.)*MU(I)
47      26 PINT=1.-FS/ST
48      RETURN
49      C COMPUTE MU CORRESPONDING TO INTEGRAL OF S1
50      ENTRY PINV(S1)
51      S1=S1*ST
52      DO 30 I=1,NTH
53      IF(S1.LE.S(I)) GO TO 32
54      30 CONTINUE
55      GO TO 36
56      32 IF(I.GT.1) GO TO 34
57      C MU>MU(I):
58      PINV=1.-(1.-MU(I))*S1/S(I)
59      RETURN
60      C MU(I-1)>MU>MU(I):
61      34 PINV=MU(I-1)+(MU(I)-MU(I-1))*(S1-S(I-1))/(S(I)-S(I-1))
62      RETURN
63      C MU<MU(NTH):
64      36 PINV=MU(I)-(1.+MU(I))*(S1-S(I))/(1.-S(I))
65      RETURN
66      END

```

APPENDIX B: FORTRAN Code for Approximate Models

```

1      REAL M,MU(19),MU0,R(19),TH(19),SP(19)
2      PI=ARCOS(-1.0)
3      C**INITIALIZE MU(I) VALUES
4      DO 1 I=1,19
5          TH(I)=(I-1)*5.
6          MU(I)=COS(TH(I)*PI/180.)
7          SP(I)=SIN(TH(I)*PI/180.)*P(MU(I),-1.,0.)
8      CONTINUE
9      C**READ ASYMMETRY FACTOR G
10     WRITE(6,110)
11     110 FORMAT('ENTER ASYMMETRY FACTOR:')
12     READ(5,112) G
13     112 FORMAT(3F10.5)
14     BF=0.
15     DO 12 I=2,18,2
16         BF=BF+SP(I-1)+4.*SP(I)+SP(I+1)
17     12 CONTINUE
18     BF=BF*PI/216.
19     14 WRITE(7,114) G,BF
20     114 FORMAT('ASYMMETRY FACTOR =',F7.3,', BACKSCATTERING FRACTION =',
21             1 F7.3,',')
22     C**READ OPTICAL THICKNESS AND ANGLE OF INCIDENCE
23     16 WRITE(6,116)
24     116 FORMAT('ENTER OPTICAL THICKNESS, ANGLE OF INCIDENCE, AND',
25             1 ' AZIMUTH:')
26     READ(5,112,FND=10) T,TH0,PHI
27     MU0=COS(TH0*PI/180.)
28     WRITE(7,122) T,TH0,PHI,(TH(I),I=1,19)
29     122 FORMAT('OPTICAL THICKNESS=',F7.3,', ANGLE OF INCIDENCE =',
30             1 F7.3,', DEGREES, RELATIVE AZIMUTH =',
31             1 F7.3,', DEGREES','/','OTH=',18(F5.2,','),F5.2)
32     X0=EXP(-T/MU0)
33     XG=EXP(-T*(1.-G)/MU0)
34     C=(1.-G)*T+(2./3.*MU0)*(1.-XG)
35     C=C/(4./3.+(1.-G)*T)
36     C**LOOP OVER ANGLES
37     DO 32 I=1,19
38         U=MU(I)
39         X=0.
40         IF(U.NE.0.) X=EXP(-T/U)
41         R1=MU0+2./3.*C+(C-1.)*U
42         R2=(C-1.)*(1.-G)*T
43         R3=(MU0*(1.-G-MU0)+P(U,-MU0,PHI)/3.)/(MU0+(1.-G)*U)
44         R(I)=R1*(1.-X)-R2*X+R3*(1.-X*XG)
45         R(I)=0.75*MU0*R(I)
46     32 CONTINUE
47     WRITE(7,132) (R(I),I=1,19)
48     132 FORMAT('ITERATED EDDINGTON MODEL','/',' R=',18(F5.3,','),F5.3)
49     C**REPEAT FOR TURNER MODEL
50     DEN=4.*(MU0+BF*T)
51     DO 34 I=1,19
52         U=MU(I)
53         X=1.
54         IF(U.NE.0.) X=1.-EXP(-T/U)
55         P1=P(U,MU0,PHI-180.)
56         P2=P(U,-MU0,PHI)
57         R(I)=(BF*(1.-U*X)*(P1+P2)+MU0*X*P2)/DEN
58     34 CONTINUE
59     WRITE(7,134) (R(I),I=1,19)
60     134 FORMAT('TURNER MODEL','/',' R=',18(F5.3,','),F5.3)

```

```

61 C**REPEAT FOR QSS MODEL
62   ON 38 I=1,19
63   U=MU(I)
64   TS=T*BF
65   YS=1.
66   IF(U.EQ.0.) GO TO 36
67   YS=1.-EXP(-TS*(1./U+1./MU0))
68   36 R(I)=P(U,-MU0,PHI)*YS*MU0/(U+MU0)/BF/4.
69   3A CONTINUE
70   WRITE(7,138) (R(I),I=1,19)
71   138 FORMAT('QSS MODEL:','0 R=',18(F5.3,', '),F5.3)
72   GO TO 16
73   END

```

```

1   FUNCTION P(MU,MU0,PHI)
2   DIMENSION TH(25),PT(25)
3   DATA TH/0.,7.5,15.,22.5,30.,37.5,45.,52.5,60.,67.5,75.,82.5,90.,
4   1 97.5,105.,112.5,120.,127.5,135.,142.5,150.,157.5,165.,172.5,180./
5   DATA PT/1000.,20.,6.,4.,3.,2.,1.,.5.,3.,2.,1.,.07.,.05,
6   1 .04.,.03.,.04.,.05.,.07.,.14.,.26.,.18.,.14.,.18.,.30.,.50/
7   REAL MU,MU0,MR
8   DEGRAD=ARCCOS(-1.0)/180.
9   MR=MU*MU0*SQRT((1.-MU*MU)/(1.-MU0*MU0))*COS(PHI*DEGRAD)
10  THETA=ARCCOS(MR)/DEGRAD
11  DO 10 I=2,25
12  IF(THETA.LE.TH(I)) GO TO 12
10 CONTINUE
14  P=PT(25)
15  12 P=PT(I)+(PT(I-1)-PT(I))*(THETA-TH(I))/(TH(I-1)-TH(I))
16  RETURN
17  END

```


REFERENCES

1. Lyzenga, D. R., Passive Remote Sensing Techniques for Mapping Water Depth and Bottom Features, Applied Optics 17, 379-383 (1978).
2. Lyzenga, D. R., Shallow Water Reflectance Modeling with Applications to Remote Sensing of the Ocean Floor, Proceedings of 13th International Symposium on Remote Sensing of Environment, 583-602 (1979).
3. Hasell, P. G. Jr., L. M. Peterson, F. J. Thomson, E. A. Work, and F. J. Kriegler, Active and Passive Multispectral Scanner for Earth Resources Applications: An Advanced Applications Flight Experiment, Report No. 115800-49-F, Environmental Research Institute of Michigan (1977).
4. Jerlov, N. G., Optical Oceanography, Elsevier Pub. Co., Amsterdam (1976).
5. Shannon, J. G., Correlation of Beam and Diffuse Attenuation Coefficients Measured in Selected Ocean Waters, Proceedings Society of Photo-Optical Instrumentation Engineering, Vol. 64, 3-11 (1975).
6. Lyzenga, D. R., R. A. Shuchman, and R. A. Arnone, Evaluation of an Algorithm for Mapping Bottom Features Under a Variable Depth of Water, Proceedings of 13th International Symposium on Remote Sensing of Environment, 1767-1750 (1979).
7. Gordon, H. R., Simple Calculation of the Diffuse Reflectance of the Ocean, Applied Optics 12, 2803 (1973).
8. Malila, W. A., R. B. Crane, C. A. Omarzu, and R. E. Turner, Studies of Spectral Discrimination, Report WRL 31650-22-T, Willow Run Laboratories (1971).
9. Young, S. J., Scattering of Solar Radiation by Clouds, Report No. SAMS0-TR-78-178, Aerospace Corporation (1978).
10. Chandrasekhar, S., Radiative Transfer, Dover Publications (1960).
11. Hansen, J. E., Exact and Approximate Solutions for Multiple Scattering by Cloudy and Hazy Planetary Atmospheres, J. Atmos. Sci. 26, 478-487 (1969).
12. Zachor, A. S., J. A. Holzer, and F. G. Smith, IR Signature Study, Report No. AFAL-TR-79-1012, Honeywell Electro-Optics Center (1979).

END

DATE
FILMED

11-8/1

DTIC